Journal of X-Ray Science and Technology 22 (2014) 213–225
DOI 10.3233/XST-140420
IOS Press

Simulation analysis of airflow alteration in the trachea following the vascular ring surgery based on CT images using the computational fluid dynamics method

Fong-Lin Chen[a,b], Tzyy-Leng Horng[c] and Tzu-Ching Shih[d,e,*]
[a]*Institute of Medicine, Chung Shang Medical University, Taichung, Taiwan*
[b]*Department of Pediatrics, Chung Shan Medical University Hospital, Taichung, Taiwan*
[c]*Department of Applied Mathematics, Feng Chia University, Taichung, Taiwan*
[d]*Department of Biomedical Imaging and Radiological Science, China Medical University, Taichung, Taiwan*
[e]*Department of Biomedical Informatics, Asia University, Taichung, Taiwan*

Received 23 February 2013
Revised 25 October 2013
Accepted 16 December 2013

Abstract. This study presents a computational fluid dynamics (CFD) model to simulate the three-dimensional airflow in the trachea before and after the vascular ring surgery (VRS). The simulation was based on CT-scan images of the patients with the vascular ring diseases. The surface geometry of the tracheal airway was reconstructed using triangular mesh by the Amira software package. The unstructured tetrahedral volume meshes were generated by the ANSYS ICEM CFD software package. The airflow in the tracheal airway was solved by the ESI CFD-ACE+ software package. Numerical simulation shows that the pressure drops across the tracheal stenosis before and after the surgery were 0.1789 and 0.0967 Pa, respectively, with the inspiratory inlet velocity 0.1 m/s. Meanwhile, the improvement percentage by the surgery was 45.95%. In the expiratory phase, by contrast, the improvement percentage was 40.65%. When the inspiratory velocity reached 1 m/s, the pressure drop became 4.988 Pa and the improvement percentage was 43.32%. Simulation results further show that after treatment the pressure drop in the tracheal airway was significantly decreased, especially for low inspiratory and expiratory velocities. The CFD method can be applied to quantify the airway pressure alteration and to evaluate the treatment outcome of the vascular ring surgery under different respiratory velocities.

Keywords: Complete vascular ring (CVR), vascular ring surgery (VRS), pressure drop, computational fluid dynamics (CFD), tracheal airway resistance

*Corresponding author: Tzu-Ching Shih, Department of Biomedical Imaging and Radiological Science, College of Health Care, China Medical University, Taichung 40402, 91 Hsueh-Shih Road, Taichung 40402, Taiwan. Tel.: +886 4 2205 3366#7709; Fax: +886 4 2208 1447; E-mail: shih@mail.cmu.edu.tw.

1. Introduction

Complete vascular rings (CVRs), congenital cardiac anomalies of the aortic arch and the vessels emerging from the heart, completely encircle the trachea and esophagus [1–3]. In general, CVR diseases are associated with the deformation problems with the tracheal stenosis and the esophageal obstruction. The major clinical symptoms of CVR often include dysphagia, stridor, chronic cough, persistent wheeze, and noisy breathing [4–7]. Based on MR images, Fleenor et al. performed the measurements of tracheal stenosis dimensions to investigate the influence of CVRs on the patient respiratory symptoms [8]. Some studies also reported that the vascular ring surgery (VRS) provides an excellent treatment to improve the patients' respiration conditions, especially for the immediate relief of symptoms [1,4,6–9]. In some patients, the compressed trachea is still collapsed even after the VRS because the trachea is malacia in nature [7,10,11]. Airway stenting may provide an immediate treatment modality for solving the tracheal malacia problem. Al-Bassam et al. presented that the thoracoscopic division of vascular rings is a safe and effective surgery rather than an open thoracotomy [9]. After a VRS, it is important to evaluate the treatment outcome of surgical relief of tracheal stenosis on those patients. However, there is little quantitative information about the airflow alteration in the trachea before and after the VRS, especially on the pressure drop analysis.

Brouns et al. applied the computational fluid dynamics (CFD) technique to explore the pressure drop in a realistic model of trachea stenosis [3]. Verbanck et al. used a force oscillation test modality for detecting the patient upper airway obstruction at different breathing airflow rates [12]. They demonstrated that the respiratory resistance is a function of breathing airflow rates and the minimal tracheal lumen area of tracheal stenosis. Tracheal stenosis can be relieved by the surgical expansion of the compressed airway. Zhang and Kleinstreuer utilized the finite volume method to analyze the particle deposition in the human upper airway at different breathing flow rates [13]. They showed that the airway deformation can affect airflow field and particle deposition pattern. Furthermore, Allen et al. used the CFD technique to simulate the air flow in the pediatric upper airway [14]. With a comparison between the experimental results and the computational data, they further reported that the CFD method can provide an accurate representation of airflow in the airway. Some studies investigated the aerosol particle transport in human airways [15–19]. Using the Weibel's lung model, Farkas and Balásházy demonstrated that the airway obstruction in the large central airway causes a redistribution of particle deposition sites [15]. Owing to the airway geometry change, the airflow pattern in the airway alters. They also found that the aerosol deposition efficiency in the abnormal narrowing airway is much higher than that in the healthy airway. It is obvious that airway obstruction affects the deposition efficiency of aerosol drug delivery. Nowak et al. suggested that the ideal Weibel model cannot predict the aerosol particle deposition for the practical conditions [16]. This is because that the model lacks the airway curvature and the airway surface irregularity to the realistic lung. Thus, in this study we use the patient-specific three-dimensional (3-D) tracheal airway (i.e., based on CT images) to simulate the air flow in the airway.

Furthermore, Malvè et al. utilized the finite element-based commercial software (ADINA R&D Inc.) to simulate the fluid structure interaction of a human trachea under different ventilation conditions [20]. They reported that the positive pressure keeps the airway open and prevents its collapse during the mechanical ventilation. The assessment of treatment outcome of the tracheal stenosis after the VRS is still little known. Therefore, the purpose of this study is not only to develop a CFD model for simulation of airflow in the patient airway but also to calculate the pressure drop under different inspiratory and expiratory velocities before and after the VRS.

Table 1
Patient data used in numerical simulation

Subject	Diagnosis	Age (years)	Sex	FEV1§		FEV1 ratio§§	Selected length Ls
				Before surgery (%)	After surgery (%)		
#1	RAA*	13	F	70	71	0.01	6.75
#2	DAA**	7	M	107	90	−0.15	5.03
#3	RAA	13	M	79	70	−0.11	5.74
#4	DAA	14	M	Nil	82	Nil	5.44
#5	RAA	13	M	102	91	−0.10	6.13
#6	RAA	7	M	82	89	0.08	6.25
#7	RAA	6	F	104	110	0.05	4.84
#8	RAA	13	M	82	82	0	6.21
#9	RAA	7	M	109	93	−0.14	4.98
#10	RAA	14	M	75	77	0.02	7.5
#11	RAA	7	F	89	85	−0.04	4.58
#12	RAA	13	M	97	103	0.06	5.94

RAA*: Right aortic arch (RAA) with left ligamentum arteriosum and Kommerell's diverticulum. DAA**: Double aortic arch (DAA). FEV1§: Forced expiratory volume in the first second of a full forced exhalation after a full inhalation. FEV1 ratio§§: (FEV1 after surgery- FEV1 before surgery)/FEV1 before surgery.

2. Materials and methods

The CFD model was tested in twelve cases in this study. Detailed clinical features of 12 patients were listed in Table 1. All these 12 patients presented with clinical symptoms of dysphagia, recurrent respiratory infections and stridor. In these patients, two had the double aortic arch (DAA), and ten had the right aortic arch (RAA) with left ligamentum arteriosum and Kommerell's diverticulum. Nine male and three female were aged of between 6 and 14 years. The average age of 12 patients was 10.58 years. The forced expiratory volume in the first second (FEV1) measurement method is often used to assess the obstruction condition of the airway. Nevertheless, in fact, the FEV1 measurement was difficult to evaluate the treatment outcome of the VRS. For instance, the FEV1 did not alter for the subject #8 before and after the VRS. In such situation, on the other hand, the FEV1 measurement would not be useful for assessing the treatment outcome of the VRS. Thus, in this study the CFD method may provide some information to the treatment outcome of the VRS. The entire process of the CFD simulation for tracheal stenosis airflow analysis can be sketched as a flow chart. In this study, the numerical simulation of air flow in the airway was performed by the four steps. Figure 1 shows the overall flowchart for modeling the air flow transportation in the trachea using the software packages and their corresponding file formats. Firstly, the tracheal airway 3-D surface geometry was reconstructed by the Amira software (Visage Imaging Inc., San Diego, CA). Secondly, the tracheal airway 3-D volume mesh generation was created using the ANSYS software (ANSYS Inc., Southpointe, Canonsburg, PA). Thirdly, the air flow was solved by the CFD-ACE+ software (ESI Group, Huntsville). Finally, the pressure drop in the airway was calculated by the CFD-VIEW software (ESI Group, Huntsville). The CFD model was tested by twelve cases.

2.1. Image acquisition and 3-D surface geometry reconstruction

All CT-scan images of twelve patients were acquired by the CT-Scanner (Philips Brilliance 40) and then saved in the Digital Imaging and Communications in Medicine (DICOM) file format. All 3-D airway geometry reconstructions were obtained from the CT images. The slice plane of acquired patient-specific CT images was considered as the x-y plane in this study (see Figs 2(b) and (d)). In this study, the slice thickness of CT images is either 0.7 mm or 1 mm. In other word, the 3-D airway geometry was

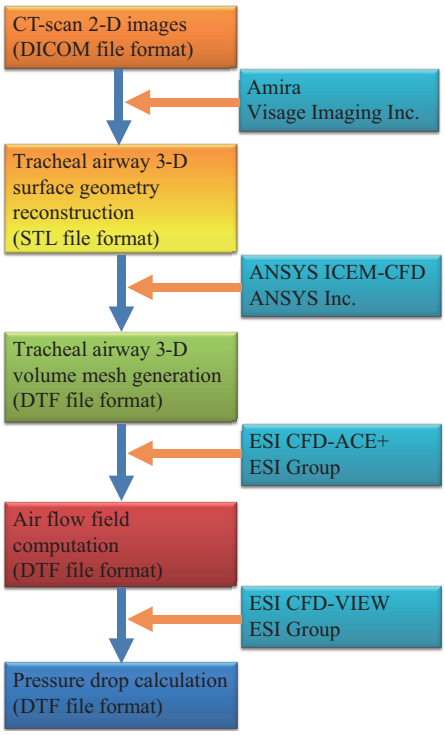

Fig. 1. The overall flowchart includes the patient-specific CT-scan images, 3-D tracheal airway geometry reconstruction, 3-D volume mesh generation of the tracheal airway, air flow field computation, pressure drop in the tracheal airway, and corresponding software tools for each stage in the computer simulation. (Colours are visible in the online version of the article; http://dx.doi.org/10.3233/XST-140420)

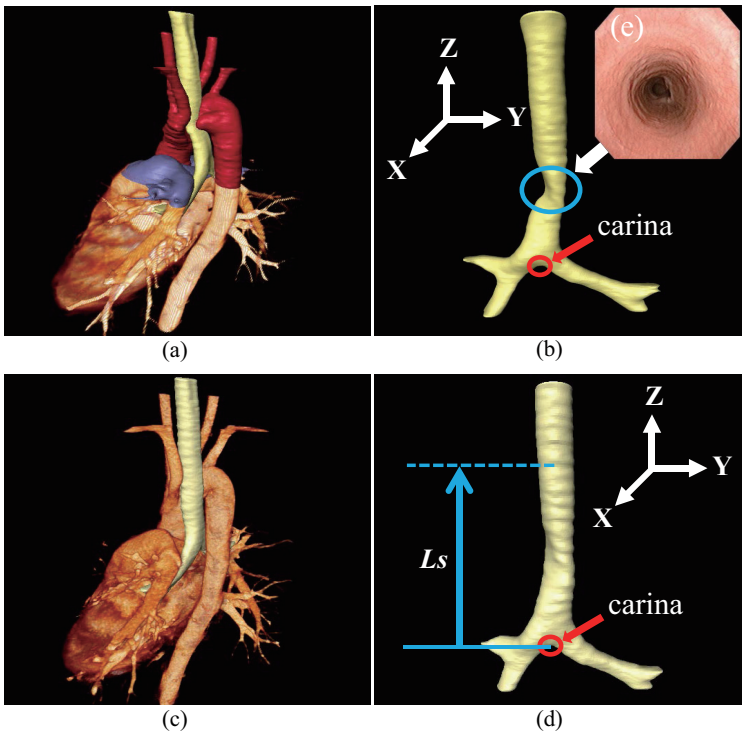

Fig. 2. Tracheal airway 3-D geometry reconstructed by the Amira software was presented for before and after the vascular ring surgery. The patient is a thirteen-year-old boy with a compressed trachea due to a vascular ring with the RAA type. The slice thickness of CT-scan images was 0.7 mm. (a)(b) for before the vascular ring surgery; (c)(d) for after the vascular ring surgery; (e) tracheal endoscopy image of a narrowed segment. Ls is the selected length of the tracheal airway for numerical simulation analysis. (Colours are visible in the online version of the article; http://dx.doi.org/10.3233/XST-140420)

also reconstructed from the CT-scan images with either 0.7 or 1 mm slice thickness in the z-axis direction. With employing the CT images in the DICOM file format, the patient-specific tracheal airway 3-D surface geometry was reconstructed by the Amira software. The tracheal airway 3-D surface geometry was rendered by using the Amira *SurfaceGen* module tool. Based on the CT-scan images, the Amira *SurfaceGen* module tool can generate the two-dimensional (2-D) triangular surface elements, which enclose completely the patient-specific tracheal airway 3-D surface. 2-D triangular surface elements overspread the tracheal airway 3-D surface. Figure 2 demonstrates the compressed airway surface reconstructed by the Amira *SurfaceGrn* module tool. Besides, the tracheal endoscopy image of a narrowed segment (i.e., the stenotic trachea) was shown in Fig. 2(e). In this study, the export file format of the Amira software was saved as the STL file format (i.e., in the stereolithography file format). Indeed, the file format between the commercial software tools is important. For instance, the export STL file format of the Amira software can be imported into the ANSYS ICEM-CFD software. With the STL data file format, the 3-D airway surface geometry was imported into the ANSYS ICEM-CFD software. The textured luminal surface of the tracheal airway (i.e. the tracheal wall) was extracted from CT-scan images in the STL file format for airway volume mesh generation.

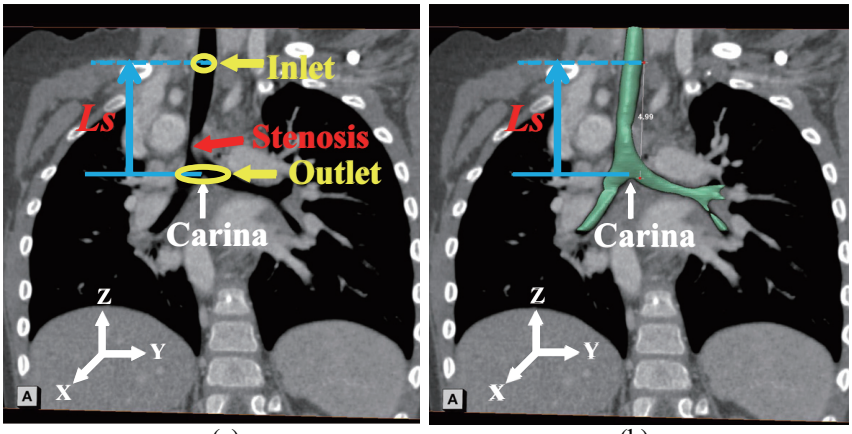

(a) (b)

Fig. 3. The cross-sectional locations of the inlet and the outlet of the subject #9 were displayed. The inlet and the outlet were displayed with the yellow arrows and used for the inspiratory time period. The tracheal stenosis indicated by the red arrow. The selected length ifrom the site of the carina was 4.99 cm. (a) CT-scan image before the vascular ring surgery; (b) tracheal airway 3-D surface combined into the CT-scan image. (Colours are visible in the online version of the article; http://dx.doi.org/10.3233/XST-140420)

2.2. *3-D volume mesh generation*

After the tracheal airway 3-D surface geometry reconstruction, the airway surface geometry was completely covered by the 2-D triangular surface elements. In other words, the luminal surface of the trachea was used as the wall boundary of tracheal airway 3-D volume mesh generation. Before volume mesh generation, the inlet and outlet surface elements were created by the ANSYS. In this study, the locations of the inlet and outlet surface were determined the anatomical location of the carina (as shown in Figs 3 and 4(b)). The cross-section allocation of the outlet was localized at the cross-sectional region passing through the carina, as displayed in Figs 3(a) and 4(b)–(g). In order to evaluate the pressure drop across the tracheal airway (i.e. tracheal airway resistance) before and after the VRS, the selected length of the trachea airway was almost the same for each case in this study. The selected length of the trachea was measured from the distance from the carina above (Figs 2(d), 3 and 4). For example, for the subject #9 the selected length was about 4.99 cm before the vascular ring surgery, as shown in Fig. 3(b). In other words, the distance between the inlet and the outlet in the z-axis direction was about 4.99 cm.

Figure 4 shows the development process of the inlet and the outlet surfaces. From the tracheal airway surface created by the Amira software, the tracheal airway surface overspread 16,348 triangular surface elements (Fig. 4(a)). We used the anatomical location of the carina to determine the two cutting planes that were used as the inlet and outlet normal planes. Based on this cutting plane referring the site of the carina, the plane curve of intersection of the selected cutting plane and the tracheal airway surface was created by the *Create/Modify Faceted* and *Repair Geometry* tools of the ANSYS ICEM CFD (Figs 4(b)–4(d)). The surface part below the carina removed (Fig. 4(b)) and the planar intersection curve (indicated by the red line in Fig. 4(d)) on the tracheal surface obtained by the *Single Curve Cleanup* tool of the ANSYS ICEM CFD. After applying the *Create/Modify Surface*module tool of the ANSYS ICEM CFD to the planar intersection curve, the normal surface plane on the tracheal airway surface was obtained, as shown in Fig. 4(e). Using this planar intersection curve, the normal surface plane passing through the carina was generated by the ANSYS ICEM CFD. This normal surface plane considered as either the outlet for inspiratory time period or the inlet for expiratory time period in simulations. Again, the

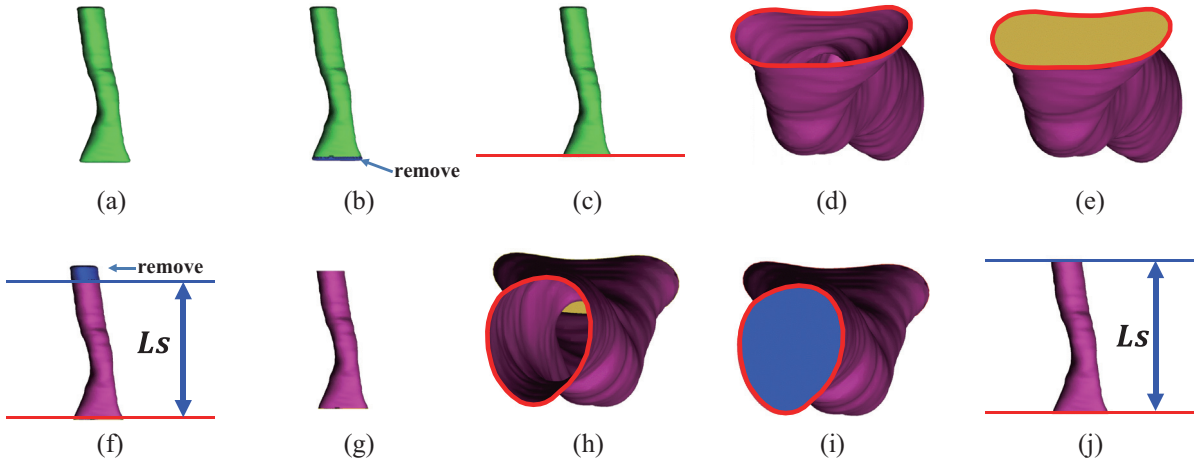

Fig. 4. The development of the inlet surface plane, the outlet surface plane and the tracheal airway surface wall was demonstrated. The tracheal airway surface of the subject #3 was overspread triangular surface elements. (a) tracheal airway surface with triangular surface elements (b) removed surface part on the tracheal airway surface; (c) the planar intersection curve indicated by the black line; (d) the planar intersection curve for creating the outlet normal surface plane for inspiratory phase; (e) the outlet normal surface plane for inspiratory phase; (f) removed surface part on the tracheal airway surface; (g) the tracheal airway surface wall; (h)the planar intersection curve on the tracheal airway surface; (i) the inlet normal surface plane for inspiratory phase. (Colours are visible in the online version of the article; http://dx.doi.org/10.3233/XST-140420)

second normal surface plane from the distance to the first normal surface plane was created, as shown in Figs 4(f)–(i). In other words, this second normal surface plane was as the inlet and the outlet for the inspiratory and expiratory time periods, respectively. Thus, the tracheal airway surface geometry consists of three surfaces, which include the inlet normal surface plane, the outlet normal surface plane, and the tracheal airway surface wall. These three surfaces were used for the 3-D solid volume mesh generation of the trachea.

In order to establish the 3-D computational gird, the volume mesh generation was performed by the commercial software ANSYS ICEM-CFD. From the tracheal airway 3-D surface geometry covered with two cutting surface planes and one tracheal airway surface wall, the tetrahedral volume mesh was generated by the *Compute Mesh*module tool of the ANSYS software and the computational grid of 3-D volume mesh of the tracheal airway was obtained. Moreover, the computational grid of the tetrahedral volume mesh was used as nodes used for solving the Navier-Stokes equations. In some cases, the computational grid quality of volume mesh affects the convergence of numerical solutions of the Navier-Stokes equations. The volume mesh can be improved by the mesh smoothing of the *Global Mesh Setup* module tool of the ANSYS ICEM-CFD. The export data format of the mesh generation by the ANSYS ICEM-CFD is the Data Transfer Facility (DTF). Note that the 3-D volume mesh was saved in the DTF file format in this study. The DTF file format can be used in the ESI CFD-ACE+ solver and the ESI CFD-VIEW post-processing software. Figure 5 shows 3-D volume mesh generation for the tracheal airway geometry before and after the VRS.

2.3. Numerical methods

With an export DTF file from the ANSYS software, the numerical computational models were imported into the ESI CFD-ACE+ software. The continuity equation is used to describe the conservative

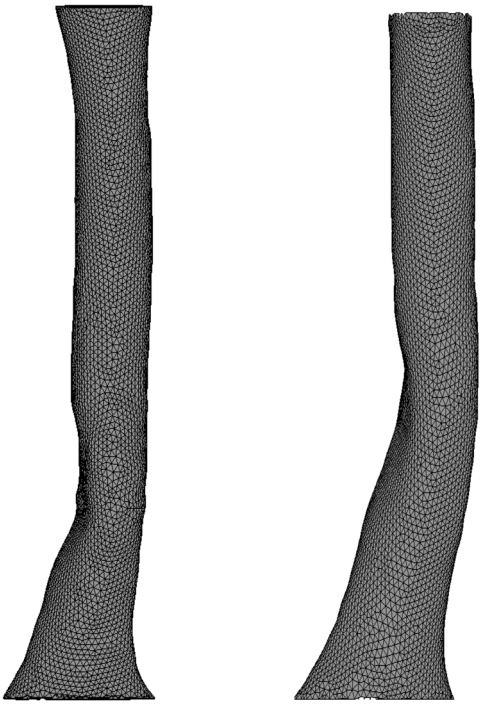

Fig. 5. 3-D volume mesh generation of the trachea by the ANSYS ICEM-CFD software (a) before the vascular ring surgery; (b) after the vascular ring surgery.

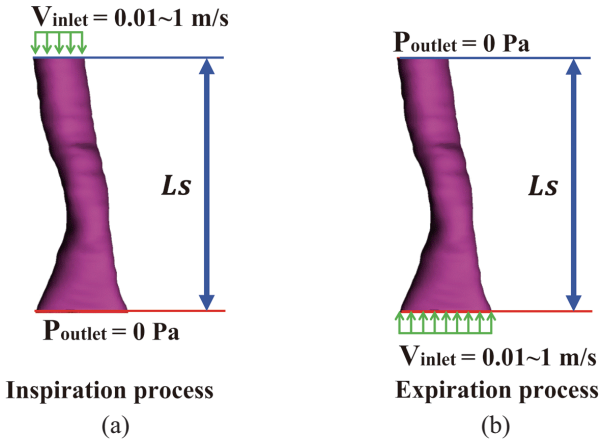

Fig. 6. Boundary conditions were imposed for breathing process simulations. (a) for inspiratory time period; (b) for expiratory time period. (Colours are visible in the online version of the article; http://dx.doi.org/10.3233/XST-140420)

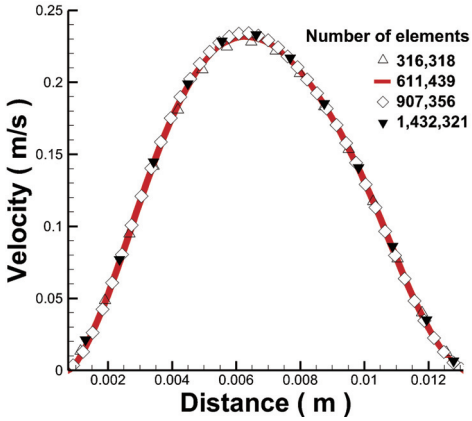

Fig. 7. The outlet velocity profiles with different element sizes at the inspiratory inlet velocity of 0.1 m/s for the subject #9. (Colours are visible in the online version of the article; http://dx.doi.org/10.3233/XST-140420)

transport of some kind of quantities such as mass, momentum, and energy. Further, the continuity equation is the local form of conservation laws. In order to investigate the transport process of airflow in the airway, the mass conservation equation and the moment equation were considered in this study.

2.3.1. Continuity equation

In fluid dynamics, the conservation equation of mass can be expressed by the continuity equation as follows:

$$\frac{\partial u}{\partial x} + \frac{\partial v}{\partial y} + \frac{\partial w}{\partial z} = 0 \tag{1}$$

where u, v, and are the velocity components in the x, y, and z directions, respectively. Moreover, van

Ertbruggen et al. used a 3-D airway model to simulate the particle deposition in airway by the CFD techniques [17]. They used the steady state air flow rate ranging from 50 to 500 cm^3/s. Based on the simulation parameters of van Ertbruggen et al. and the average velocity on the cross-sectional area of the airway (i.e., the averaged cross-sectional area was about 0.5 cm^2), the velocity of air flow was varied between 0.1 m/s and 1 m/s for simulations. For example, for the inlet cross-sectional area of 0.71 cm^2, the Reynolds numbers roughly range from 5.14 to 514.67 when the inspiratory inlet velocity varies from 0.01 m/s to 1 m/s. Similarly, the Reynolds numbers of these 12 patients was small. In this study, we used the air flow pattern in the tracheal airway as the laminar flow in numerical simulations.

2.3.2. Momentum equation

The conservation equations of momentum were described by the well-known Navier-Stokes equations as follows:

$$\rho\left(\frac{\partial u}{\partial t}+u\frac{\partial u}{\partial x}+v\frac{\partial u}{\partial y}+w\frac{\partial u}{\partial z}\right)+\frac{\partial p}{\partial x}=\mu\left(\frac{\partial^2 u}{\partial x^2}+\frac{\partial^2 u}{\partial y^2}+\frac{\partial^2 u}{\partial z^2}\right)+\rho g_x \tag{2}$$

$$\rho\left(\frac{\partial v}{\partial t}+u\frac{\partial v}{\partial x}+v\frac{\partial v}{\partial y}+w\frac{\partial v}{\partial z}\right)+\frac{\partial p}{\partial y}=\mu\left(\frac{\partial^2 v}{\partial x^2}+\frac{\partial^2 v}{\partial y^2}+\frac{\partial^2 v}{\partial z^2}\right)+\rho g_y \tag{3}$$

$$\rho\left(\frac{\partial w}{\partial t}+u\frac{\partial w}{\partial x}+v\frac{\partial w}{\partial y}+w\frac{\partial w}{\partial z}\right)+\frac{\partial p}{\partial z}=\mu\left(\frac{\partial^2 w}{\partial x^2}+\frac{\partial^2 w}{\partial y^2}+\frac{\partial^2 w}{\partial z^2}\right)+\rho g_z \tag{4}$$

where t is the time, ρ is the density of air, μ is the pressure, is the air viscosity. The components of the gravitational acceleration in the, x, y, and z directions are denoted by g_x, g_y, and g_z, respectively. In this study, the 2-D plane of acquired CT-scan images was referred to as the X-Y plane in the 3-D reconstruction of the trachea. So the 3-D tracheal airway geometry was reconstructed along the Z-axis direction (i.e. the gravitational body force can thought as along the Z-axis direction), which was parallel to the gravitational direction. In other words, the gravitational body force is in the Z-axis direction in CFD simulations. The gravitational body force was ignored due to a short trachea (i.e., the z-direction length of the trachea used in simulation is less than 6 cm). Note that the gravitational acceleration term was neglected in numerical simulations. The above differential equations were implemented in each node of the 3-D mesh. Moreover, in this study the gravitational effect was ignored. In numerical simulations, the uniform inhaled velocity flow of air was imposed at the inlet of the trachea for the inspiration time period. Note that in this numerical simulation the density of air is 1.1614 kg/m^3 and the viscosity of air is 1.846×10^{-5} kg/m/s. The no-slip boundary conditions were applied on the tracheal airway interior wall and a uniform velocity profile was used at the inlet.

It should be noted that the changes of viscous pressure drop starts from the carina in which the trachea braches at the carina into the left and right main stem bronchi, as shown in Figs 2(b) and (d). With the length L_s above the carina, the viscous pressure drop in the selected segment of the tracheal airway is used for evaluating the airway resistance for a respiration process using by the CFD techniques. In the numerical simulations with the CFD-ACE solver, the iterations were continued until the residuals for each of the equations (each component of the continuity and the Navier-Stokes equations) dropped to at least 10^{-6} of the maximum value. Air flow transport in the selected segment of the narrowing airways within the discrete computational domain was described by the CFD-ACE+ (i.e., the finite volume Navier-Stokes solver). In other words, the numerical solutions of the flow-governing equations (i.e., the Navier-Stokes equations) were solved by the CFD-ACE+ software packages. Using the image

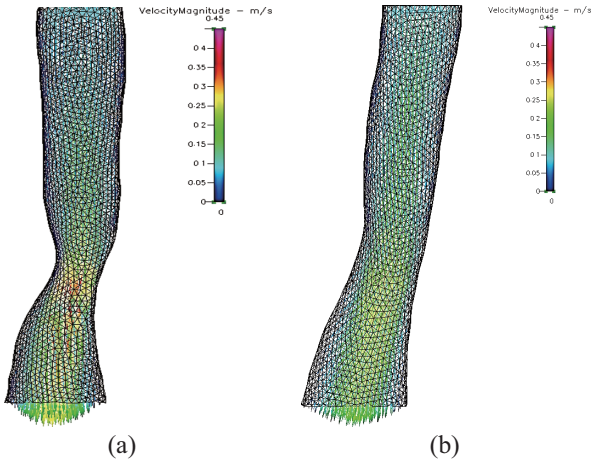

Fig. 8. The velocity distribution in the tracheal airway for the inspiratory inlet velocity of 0.1 m/s. (a) before the vascular ring surgery; (b) after the vascular ring surgery. (Colours are visible in the online version of the article; http://dx.doi.org/10.3233/XST-140420)

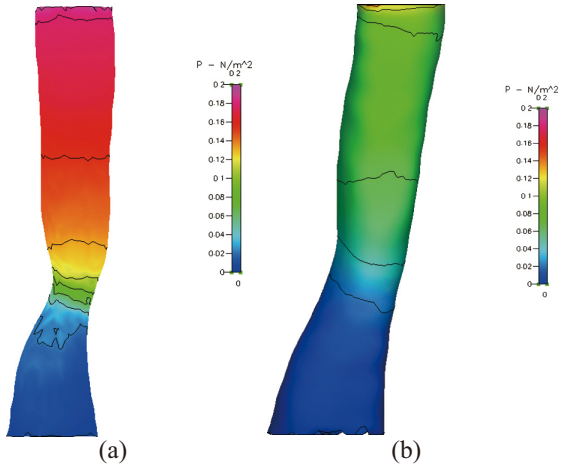

Fig. 9. The pressure distribution for the inspiratory velocity of 0.1 m/s. (a) before the vascular ring surgery; (b) after the vascular ring surgery. (Colours are visible in the online version of the article; http://dx.doi.org/10.3233/XST-140420)

reconstruction and the CFD techniques, the viscous pressure drop in the compressed segment of the trachea can be calculated for patient inspiration and expiration activities before and after the VRS. The three velocity values (i.e., 0.01, 0.1, and 1 m/s) were employed for simulation of the patients' respiratory activities, which includes expiration and inspiration. In addition, in this study the three inlet velocities were presented as three different activities such as rest, mild, and excise conditions with 0.01, 0.1, and 1 m/s, respectively.

2.3.3. Boundary conditions

Figure 6 shows the boundary conditions in this study. The inlet boundary used constant velocity condition and flat velocity profile. The outlet boundary employed constant pressure condition and assigned to the zero pressure [21–24]. The boundary condition of the tracheal airway interior wall was applied with a no-slip condition. For the inspiratory time period, the inlet was applied to the upper end away from the carina (Fig. 6(a)). For the expiratory time period, by contrast, the inlet was applied to the lower end nearby the carina (Fig. 6(b)). Furthermore, the inlet, the outlet and the tracheal airway interior wall boundary conditions were as *Inlet*, *Outlet*, *Wall BC Type*s in the ESI CFD-ACE+. The grid independent test was performed, as illustrated in Fig. 7. The velocity profile at the outlet of the airway was demonstrated for different grid sizes. For the inlet inspiratory velocity of 10 cm/s, the grid independency analysis was carried out with the grid size from 316,318 to 1,432,321. The numerical solution is nearly independent of grid sizes in this simulation study.

3. Results

We applied the CFD techniques to calculate the pressure changes across the tracheal stenosis with the selected length at inlet velocities of 0.01, 0.1, and 1 m/s for inspiration and expiratory phases before and after intervention. After the VRS, the cross-sectional area of the compressed narrowing trachea became larger. Figure 8 shows that the maximum velocity occurs in the narrowing tracheal airway is higher than

Table 2
Pressure changes before and after the VRS for three different velocities for the subject #2

	Inspiration			Expiration		
Velocity (m/s)	0.01	0.1	1	0.01	0.1	1
Air flow rate $\times 10^{-7}$ (m^3/s)	7.08964	70.8964	708.964	7.08964	70.8964	708.964
Pressure drop (Pa)						
Before surgery	0.01187	0.17899	4.98804	0.01386	0.20519	6.01835
After surgery	0.00672	0.09673	2.82711	0.00858	0.12176	3.82141

Table 3
Pressure drops for twelve patients before and after the VRS

Subject		Inspiration			Expiration		
	Inlet velocity (m/s)	0.01	0.1	1	0.01	0.1	1
	Pressure drop (Pa)						
#1	Before	0.00705	0.10997	3.75986	0.00816	0.1222	3.99681
	After	0.00446	0.05988	1.7641	0.00537	0.07591	2.48064
#2	Before	0.01187	0.17899	4.98804	0.01386	0.20519	6.01835
	After	0.00672	0.09673	2.82711	0.00859	0.12177	3.82141
#3	Before	0.00551	0.08809	2.16687	0.00549	0.08352	2.03339
	After	0.00385	0.06406	2.07446	0.00374	0.05855	1.77921
#4	Before	0.00312	0.05043	1.23923	0.00373	0.0667	1.92783
	After	0.00242	0.03682	0.89658	0.00278	0.04498	1.28007
#5	Before	0.00557	0.08983	2.65021	0.00669	0.10486	3.31614
	After	0.00441	0.07274	2.28621	0.0057	0.09059	3.1796
#6	Before	0.00538	0.0713	1.93535	0.00666	0.09092	2.82785
	After	0.00426	0.05761	1.65364	0.0051	0.07368	2.55767
#7	Before	0.00659	0.08682	2.36422	0.0079	0.10748	3.30658
	After	0.00546	0.07276	1.96351	0.00661	0.09183	2.94667
#8	Before	0.0031	0.05253	1.39859	0.00386	0.06606	2.35958
	After	0.00305	0.05209	1.42617	0.0037	0.06427	2.36202
#9	Before	0.00688	0.09803	2.21652	0.00801	0.11622	3.25657
	After	0.00575	0.08709	2.12052	0.0007	0.10564	3.21989
#10	Before	0.00566	0.0892	3.2215	0.00725	0.10943	3.89028
	After	0.0031	0.0476	1.77406	0.00445	0.06803	2.59337
#11	Before	0.00421	0.06231	1.59399	0.00495	0.078	2.68089
	After	0.00336	0.04611	0.99642	0.00418	0.06265	2.08244
#12	Before	0.04332	0.07513	1.92384	0.0052	0.08931	2.95591
	After	0.00366	0.06253	1.9623	0.00467	0.07812	2.81406

that in the preoperative trachea at the same inspiration inlet velocity 0.1 m/s for the subject #2. When the inspiratory velocity was at 0.1 m/s, the maximum velocity in the compressed trachea was about at 0.4262 m/s, as shown in Fig. 8(a). By contrast, the maximum velocity in the airway before the VRS was around 0.294 m/s for the same inspiration (i.e., inlet) velocity of 0.1 m/s. Moreover, Table 2 shows the pressure change for different velocities before and after the VRS. For the inspiration velocity of 0.1 m/s, the pressure drop was 0.17899 Pa before the VRS. After the VRS, the pressure reduced to 0.09673 Pa. Meanwhile, the airway resistance was approximately reduced to 54.04% after the vascular ring surgery. Table 3 listed the pressure changes across the selected lengths of the tracheal airways for the twelve cases for the inlet velocity ranging from 0.01 to 1 m/s before and after the VRS. Moreover, it is difficult to evaluate the outcome of the surgery by the FEV1 examination. For example, for the subject #8 the FEV1 was the same before and after the VRS. In this case, the FEV1 measurement method cannot assess the

Table 4
Univariate analysis of improvement percentages under different inlet velocities and physical activities

Physical activity	Inlet velocity (m/s)	N	Improvement percentage (%)		p-value[1]	p-value[2]	p-value[3]
			Mean $\pm$ SD	Median (IQR)			
Inspiration	0.01	12	30.6 ± 22.8	21.8 (21.2)	< 0.001	< 0.001	< 0.001
	0.1	12	25.1 ± 14.6	22.6 (19.9)	< 0.0001	< 0.001	< 0.001
	1	12	21.4 ± 19.4	15.8 (36.1)	0.003	0.039	0.002
Expiration	0.01	12	28.7 ± 22.7	24.5 (20.9)	0.001	< 0.001	< 0.001
	0.1	12	22.5 ± 12.8	19.3 (22.1)	< 0.0001	< 0.001	< 0.001
	1	12	17.2 ± 14.7	11.7 (29.0)	0.002	0.006	0.001

N: number of subjects; SD: standard deviation; IQR: interquartile range; [1]t-test; [2]Wilcoxon sign-rank test; [3]Sign test (exact test).

Table 5
Repeated measures analysis of variance (ANOVA)

Source of variation	df	Inspiration			Expiration		
		SS	F-value	p-value	SS	F-value	p-value
Subjects	11						
Velocities	2	70.11	94.73	< 0.0001	130.54	141.57	< 0.0001
Operations	1	0.90	8.53	0.0139	0.84	9.91	0.0093
Subjects $\times$ velocities	22	8.14			10.14		
Subjects $\times$ operations	11	1.17			0.93		
Velocities $\times$ operations	2	1.58	8.01	0.0024	1.48	9.56	0.001
Residual	22	2.17			1.70		
Total	71						

df: Degrees of freedom; SS: Sum of squares.

outcome of the vascular ring surgery. However, the CFD method may provide more information. For the subject #8, for instance, the pressure drops before and after intervention were 0.0031 Pa and 0.00305 Pa for the inspiratory inlet velocity of 0.01 m/s. After the VRS, the tracheal airway resistance (i.e., pressure drop) became smaller when the inspiratory inlet velocity was 0.01 m/s. However, the tracheal airway resistance increased when the inspiratory inlet velocity was 1 m/s. In the meantime, the pressure drops were 1.39859 Pa and 1.42617 Pa before and after the VRS, respectively. In numerical simulations, the pressure drop (i.e., airway resistance) for expiratory phase was larger than that for inspiratory phase (Table 3). Riazuddin et al. have reported the similar phenomenon [25]. They suggested that turbulence intensity was more predominant during expiratory phase, where vortex formation could be observed only during the inspiratory phase. In this numerical study, we found that the pressure drop during the expiratory phase was higher than that during the inspiratory phase.

Table 4 lists the improvement percentages with different inhaled velocities such as 0.01 m/s, 0.1 m/s, and 1 m/s. On univariate analysis, during the inspiration period the improvement percentages of the patient with treatments were significant for the inlet velocities of 0.01 m/s ($p < 0.001$), and 0.1 m/s ($p < 0.001$). Furthermore, for the high inlet velocity 1 m/s the improvement percentages were about 21.4 (Mean $\pm$ SD), and 15.8 (Median) in inspiration activity. Similar trends were noted in expiration activity.

Table 5 shows that using a repeated measure analysis of variance (ANOVA) for improvement percentage analysis. Table 2 also displays the improvement percentages of inspiration and expiration activities for the twelve patients after vascular ring surgeries. After a surgical treatment for vascular ring, the pressure drop in the airway decreased because of the compressed airway relieved. With comparison of inspiration and expiration activities, the improvement percentage of inspiration is higher than that of expiration, especially for a low inlet velocity.

4. Discussion

Here this study demonstrates that the CFD method can used to simulate the influence of the airflow in the airway on airflow resistance analysis. The airflow, passing through the narrowed tracheal airway, needs higher pressure to overcome the viscous resistance due to the tracheal stenosis. In numerical simulation results, the pressure drop was higher during the expiratory time period (Table 3). Moreover, the pressure drop in the tracheal airway increased while the inlet velocity was increasing. Higher pressure drop has larger flow resistance. In other words, the narrowed tracheal airway could result in a higher flow resistance (i.e., larger pressure drop in the same selected length of the trachea before the VRS). For the inspiratory inlet velocity of 1 m/s and the selected length of 6.75 cm, for example, the pressure drop before the VRS was 3.75986 Pa for subject #1 (Table 3). After VRS, the pressure drop became small about 1.7641 Pa. Figure 9 demonstrates the pressure distributions for the inspiratory inlet velocity of 0.1 m/s. Table 3 shows that the pressure drops after the VRS is higher than that before one (i.e., with tracheal stenosis), except the subjects #8, #9 and #12. On the other hand, the driving pressure before the VRS required larger than that after one for the same air flow rate. Figure 9 further shows that the pressure in the narrowed airway is higher than that that of preoperative one. Additionally, the pressure change of the compressed segment for preoperative surgery is more rapid than that of preoperative one, as shown in Figs 9(a) and (b). Case #8 has no change in the physiological FEV1 measurement before and after surgery, as shown in Table 5. Table 5 also shows that the pressure changes in this case are also very small comparing to other cases such as Cases #1 and #10 (Table 1 and Table 5). The changes are likely to be insignificant (due to the noise). Hence, it seems that CFD method is in agreement with the FEV1 testing method.

5. Conclusions

This study presents a CFD approach as a useful tool for evaluation of the pressure drop at different velocities before and after the surgery. This CFD method proved the airway flow resistance of tracheal stenosis caused by CVR can be augmented by increased air flow velocity. By the findings of the viscous pressure drop in the tracheal airway decreases significantly after surgical relief of the compressed tracheal airway, CFD approach can be a useful method for evaluating the effectiveness of VRS on relief of tracheal stenosis.

Acknowledgment

This work was supported by the National Science Council of Taiwan under grant NSC 100-2221-E-039-002-MY3 and by China Medical University under grant CMU101-S-05 (101514C*).

Authors' contributions

TCS worked on the image reconstruction from CT scan images, CFD modeling implementation, analyzed the numerical simulation results, and drafted the manuscript. TLH checked the method procedure and analyzed the numerical results. FLC conceived the study, helped to interpret the simulation results and participated in the data analysis. All authors read and approved the final manuscript.

Competing interests

None.

References

[1] R.E. Gross, Surgical relief for tracheal obstruction from a vascular ring, *The New England Journal of Medicine* **233** (1945), 586–590.

[2] F.S. Idriss, S.Y. DeLeon, M.N. Ilbawi, C.R. Gerson, G.F. Tucker and L. Holinger, Tracheoplasty with pericardial patch for extensive tracheal stenosis in infants and children, *The Journal of Thoracic and Cardiovascular Surgery* **88** (1984), 527–536.

[3] M. Brouns, S.T. Jayaraju, C. Lacor, J. De Mey, M. Noppen, W. Vincken and S. Verbanck, Tracheal stenosis: A flow dynamics study, *Journal of Applied Physiology* **102** (2007), 1178–1184.

[4] P.J. Pickhardt, M.J. Siegel and F.R. Gutierrez, Vascular rings in symptomatic children: Frequency of chest radiographic findings, *Radiology* **203** (1997), 423–426.

[5] A. Turner, G. Gavel and J. Coutts, Vascular rings-presentation, investigation and outcome, *European Journal of Pediatrics* **164** (2005), 266–270.

[6] Y. Suematsu, B.N. Mora, T. Mihaljevic and P.J. del Nido, Totally endoscopic robotic-assisted repair of patent ductus arteriosus and vascular ring in children, *The Annals of Thoracic Surgery* **80** (2005), 2309–2313.

[7] A. Bonnard, F. Auber, L. Fourcade, V. Marchac, S. Emond and Y. Révillon, Vascular ring abnormalities: A retrospective study of 62 cases, *Journal of Pediatric Surgery* **38** (2003), 539–543.

[8] J.T. Fleenor, P.M. Weinbrg, S.S. Kramer and M. Fogel, Vascular rings and their effect on tracheal geometry, *Pediatric Cardiology* **24** (2003), 430–435.

[9] A. Al-Bassam, M.S. Mallick, A. Al-Qahtani , T. Al-Tokhais, A. Gado, A. Al-Boukai, A. Thalag and M. Alsaadi, Thoracoscopic division of vascular rings in infants and children, *Journal of Pediatric Surgery* **42** (2007), 1357–1361.

[10] J.D. Finder, Understanding airway disease in infants, *Current Problems in Pediatrics* **29** (1999), 65–81.

[11] K.A. Carden, P.M. Boiselle, D.A. Waltz and A. Ernst, Tracheomalacia and tracheobronchomalacia in children and adults: An in-depth review, *Chest* **127** (2005), 984–1005.

[12] S. Verbanck, T. de Keukeleire, D. Schuermans, M. Meysman, W. Vincken and B. Thompson, Detecting upper airway obstruction in patients with tracheal stenosis, *Journal of Applied Physiology* **109** (2010), 47–52.

[13] Z. Zhang and C. Kleinstreuer, Airflow structures and nano-particle deposition in a human upper airway model, *Journal of Computational Physics* **198** (2004), 178–210.

[14] G. Allen, B. Shortall, T. Gemci, T. Corcoran and N. Chigier, Computational simulations of airway in an in vitro model of the pediatric upper airways, *ASME Transactions Journal of Biomechanical Engineering* **126** (2004), 604–613.

[15] Á. Farkas and I. Balásházy, Simulation of the effect of local obstructions and blockage on airflow and aerosol deposition in central human airways, *Journal of Aerosol Science* **38** (2007), 865–884.

[16] N. Nowak, P.P. Kakade and A.V. Annapragada, Computational fluid dynamics simulation of airflow and aerosol deposition in human lungs, *Annals of Biomedical Engineering* **31** (2003), 374–390.

[17] C. van Ertbruggen, C. Hirsch and M. Paiva, Anatomically based three-dimensional model of airways to simulate flow and particle transport using computational fluid dynamics, *Journal of Applied Physiology* **98** (2005), 970–980.

[18] P.W. Longest and S. Vinchurkar, Effects of mesh style and grid convergence on particle deposition in bifurcating airway models with comparisons to experimental data, *Medical Engineering and Physics* **29** (2007), 350–366.

[19] E.G. Meraz, H. Nazeran, C.D. Ramos, P. Nava, B. Diong and M.D. Goldman, Analysis of impulse oscillometric measures of lung function and respiratory system model parameters in small airway-impaired and healthy children over a 2-year period, *BioMedical Engineering OnLine* **10** (2011), 21.

[20] M. Malvè, A.P. del Palomar, A. Mena, O. Trabelsi, J.L. López-Villalobos, A. Ginel, F. Panadero and M. Doblaré, Numerical modeling of a human stented trachea under different stent designs, *International Communications in Heat and Mass Transfer* **38** (2011), 855–862.

[21] Y. Liu, R.M.C. So and C.H. Zhang, Modeling the bifurcating flow in an asymmetric human lung airway, *Journal of Biomechanics* **36** (2003), 951–959.

[22] C.Y. Ho, H.M. Liao, C.Y. Tu, C.Y. Huang, C.M. Shih, M.Y.L. Su, J.H. Chen and T.C. Shih, Numerical analysis of airflow alteration in central airways following tracheobronchial stent placement, *Experimental Hemotology & Oncology* **1** (2012), 23.

[23] H.Y. Luo and Y. Liu, Modeling the bifurcating flow in a CT-scanned human lung airway, *Journal of Biomechanics* **41** (2008), 2681–2688.

[24] T.C. Shih, H.D. Hsiao, P.Y. Chen, C.Y. Tu, T.I. Tseng and Y.J. Ho, Study of pre-and post-stent implantation on tracheal airway using CFD, *Journal of Medical and Biological Engineering*, in press, 2014.

[25] V.N. Riazuddin, M. Zubair, M.Z. Abdullah, R. Ismail, I.L. Shuaib, S.A. Hamid and K.A. Ahmad, Numerical study of inspiratory and expiratory flow in a human nasal cavity, *Journal of Medical and Biological Engineering* **31** (2011), 201–206.